Mechanism and Machine Theory 44 (2009) 559–579

Contents lists available at ScienceDirect

Mechanism and Machine Theory

journal homepage: www.elsevier.com/locate/mechmt

Bio-inspired design of electrically-driven bounding quadrupeds via parametric analysis

Panagiotis Chatzakos, Evangelos Papadopoulos *

Department of Mechanical Engineering, National Technical University of Athens, 9 Heroon Polytechniou Street, Athens 157 80, Greece

ARTICLE INFO

Article history:
Received 11 November 2007
Received in revised form 23 July 2008
Accepted 26 August 2008
Available online 7 October 2008

Keywords:
Systematic design
Quadruped robot
Dynamic running
Parametric analysis

ABSTRACT

This paper attempts to set the basis for a systematic approach in designing quadruped robots employing a dynamically stable quadruped running in the sagittal plane with a bounding gait, which is a simple model commonly used to analyze the basic qualitative properties of quadruped gaits that use the legs in pair. The outcome of the proposed methodology is the optimal *shape* of the bounding quadruped robot, i.e., the relation between its physical parameters, and the optimal *size* of the bounding quadruped robot, i.e., the physical magnitude of it, according to desired performance criteria. The performance criterion introduced is based on: (a) the actuator effort to sustain an active gait, very close to a passive one, and (b) the maximum payload capability of the robot for a target overall mass. The parametric study examines the behavior of the performance criterion over a range of non-dimensional variables connected to robot physical parameters and gait characteristics. The study takes into consideration data from experimental biology and ground surface properties, while it is subject to the existing technological limitations and economic restraints, i.e., the fact that there is a limited number of motor/gearbox combinations available from a practical point of view. The findings from simulation results indicate that the proposed methodology can assist in the design of new, and modifications of existing quadruped robots.

1. Introduction

A number of quadruped robots, capable of dynamically stable running, have been built with very different physical parameters. Some of these include the MIT quadruped [1], the KOLT [2], the Scout [3], the BigDog [4], PAW [5], Rush [6] and the Tekken [7]. Unlike statically stable robots, dynamically stable robots can tolerate departures of the center of mass from the support polygon formed by the legs in contact with the ground. Despite considerable research work and a large number of publications, the interesting issue of the systematic quadruped robot design remains still relatively untouched. At best, biological data has been used to aid selection of the basic robot physical parameters, such as body length, leg stiffness and hip height. Also, the influence of robot physical parameters on key quantities of robot performance, such as actuator effort and payload capability, is not fully explored. Initial simulation results presented in this paper show that the effect of these parameters is great and that considerable variations exist on the values of actuator effort and payload capability, that make some parametric regions more desirable than others, and thus their study can facilitate improved quadruped robot design.

Some work in this direction was done in [8], where scaling concepts for bounding quadrupeds were discussed. Just like shapes can be geometrically similar, movements may be dynamically similar. Two moving bodies are dynamically similar if

* Corresponding author. Tel.: +30 210 772 1440; fax: +30 210 772 1455.
E-mail address: egpapado@central.ntua.gr (E. Papadopoulos).

0094-114X/$ - see front matter © 2008 Elsevier Ltd. All rights reserved.
doi:10.1016/j.mechmachtheory.2008.08.007

the motion of one can be made identical to that of the other by multiplying all linear dimensions by one constant, time intervals by another constant and forces by a third constant [9]. Particularly in [8], dynamically similar motions obtained for a wide range of a robot physical parameters and gait characteristics. Certain parametric regions, from all possible, are more desirable than others according to specific performance criteria, and thus a particular (optimal) combination of physical parameters can be chosen. However, the important question about the relative magnitude (the scale) of the quadruped robot is not addressed in [8]. In simpler words: "How big the quadruped robot should be?"

It is generally accepted that the performance of different subsystems may scale differently, which is even more important in complex systems, such as legged robots. Parametric analysis of the ways in which different subsystems scale, permits conclusions to be drawn about the necessity for configuration changes. Also, non-dimensional numbers that combine important system parameters are particularly useful when dealing with systems that have similar configuration but different scale. For example, the Reynolds number in fluid mechanics is an indicator of the onset of turbulence [10]. Similarity analysis and its role in experimental mechanics is also well established in engineering practice. A relevant example of a scaling law is provided by the Froude number [11]. Particularly in legged locomotion, the Froude number has been shown to be a predictor of dynamic gait transitions in animals of widely differing size; that is, animals will tend to transition from a walk to a trot, and from a trot to a gallop at similar values of the Froude number [12]. It important to note that dimensional analysis is a remarkable tool in so far as it can be applied to any and every quantitative model, no matter how complex the physical model is. Apparently, when the number of differential equations used to describe a physical model is great, dimensional analysis will probably be of less value. Further, while the individual dimensionless equations might be different if one uses different normalization parameters instead, the relationships between them would be invariant. To this end, dimensional analysis is employed for this study to broaden our analysis and reveal the effect of scaling in determining robot physical parameters.

In this paper, this answer to the question about the optimal size of the quadruped robot is inferred from the performance of a similarly configured bounding quadruped, but scaled to a smaller or larger size. Specifically, the actuator effort required to sustain an active motion, which is very close to a passive one, determines the minimum size of the robot actuators and connects the size of the motor drive(s) to the size of the legged robot. The actuator effort determined corresponds to the maximum speed and torque requirements in the bounding cycle, i.e., the most demanded values are taken into account. Unveiling of how the actuator effort required to sustain motion changes across the parametric range of the robot physical parameters and motion characteristics, provides valuable insight into quadruped robot design and sets the basis for a methodology that could assist with the design, as well as the modification, of quadruped robots.

The robot in our study is purposely simple and incorporates basic elements that are found in the majority of legged robots. Each leg of the robot has a prismatic joint with a linear spring to provide compliance, and each hip is actuated. By using a simpler model, the conclusions of the parametric study are more general than they would be from studying a more specific robot case. Note that virtually all quadruped robots that are capable of dynamic locomotion, which is our focus, have a hip joint, a hip actuator and some sort of passive compliance in the leg, as does the robot studied here. Simplified models [13], and passive dynamics [3], already have been proved to be helpful in designing controllers that result in considerable energy savings [14,15]. The model used in this paper is similar to the planar models used in [1,3,6–8], which have successfully demonstrated the dynamic properties of quadruped gaits that use the legs in pair, such as the trot, the pace, the bound, the pronk, and it includes pitching. Also, it is unactuated and conservative, so that the properties of the natural dynamics of the system can be revealed. It encodes the targeted task-level behavior (steady state bounding) of the quadruped robot and reveals intrinsic system properties and aspects of quadrupedal running that are anticipated to be used for the improved design of quadruped robots.

Further, we are interest in the bounding gait; the reason is twofold. First, biologists' predicted energy-saving galloping speed of living quadrupeds [16], has not been surpassed by their robotic counterparts. To our best knowledge, Raibert's quadruped is the fastest four-legged running machine built to date, capable of bounding at 2.9 m/s [1], which is however hydraulically driven, while RHex [17], the fastest (body lengths per second) legged robot that is propelled by electric drives, has achieved a maximum forward speed of 2.7 m/s. Second, bounding, which is found mainly in small, non-cursorial animals, may occasionally be used by cursors, as well, for locomotion over difficult terrain and for moderate-speed running [18]. Bounding as a quadruped gait for robotic locomotion has been successfully demonstrated two decades ago already by Marc Raibert, the inventor of legged robots; see [1]. If the control of the system can make the two front and the two back legs work together as though they were one leg at the back and one leg at the front, then the quadruped can be controlled like an equivalent biped. Once this is done, one-legged control approaches can be used. This concept is called the virtual leg [1]. This approach relaxes the need for considering the supporting pattern in 3D, which is at least a triangle formed by three or four supporting legs.

Lastly, this work is focused on small-scale, where electric power is the predominant source of energy, and thus small-scale electric actuators were considered in the parametric analysis. Most of the legged robots capable of dynamically stable running that have been built to date have used electromagnetic motors for propulsion [2,3,5–7,17,19]. Initially, simple scaling laws are derived from first principles where the basis for these laws is obvious and then electric scaling laws are developed following certain techniques, which are discussed comprehensively. The developed electrical scaling laws examine resistive, magnetic, and electrostatic effects, as in [20], and they are verified by using data from commercial systems. Combining the simple scaling laws with each other and with engineering relationships produces more complex and less intuitive laws. Applications of the scaling laws are then used to provide direction aiming at improved quadruped robot design.

2. Dynamic modelling

The complexity of four-legged animals and robots can be reduced to relatively simple models, that can then be used to analyze a system's behavior, by taking into account *synergies*, i.e. parts that work together in coordinated action or operation, and *symmetries*, i.e. the correspondence of parts on opposite sides of a plane through body [13]. Such a simple model, which is commonly used to analyze the basic qualitative properties of quadrupedal running in the sagittal plane, is shown in Fig. 1, while its associated parameters needed to describe it are given in Table 1.

As shown in Fig. 1, the planar model represents the lateral half of a quadruped, and consists of a rigid body and two springy massless legs, attached to either side of the body (at the front and the rear). Actuators control the angle of each leg with respect to the body and the torque delivered by each leg. Each modelled leg represents the back or the front *leg pair*, in which the two back or front legs are always in phase and is called the *virtual leg* [1]. Each virtual leg has twice the stiffness

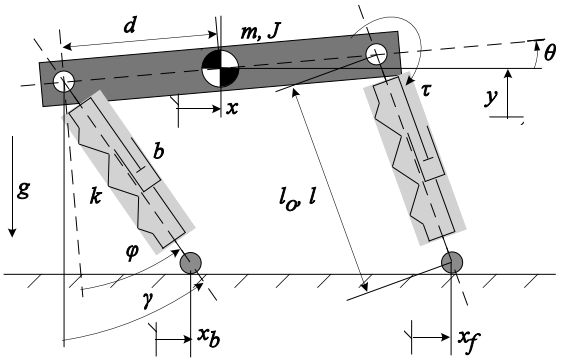

Fig. 1. Parameters of the template for quadrupedal bounding in plane.

Table 1
Variables and indices used

Symbol	Units	Variable
x	m	COM horizontal pos.
y	m	COM vertical pos.
θ	°	Body pitch angle
γ	°	Leg absolute angle
ϕ	°	Leg relative angle
x_{bt}	m	Back toe horizontal pos.
x_{ft}	m	Front toe horizontal pos.
l	m	Leg length
l_o	m	Leg rest length
k	Nt/m	Leg spring stiffness
τ	Nt/m	Torque delivered at hip
F	Nt	Axial force at leg
f_{fr}	Nt	Overall friction force
f_c	Nt	Coulomb friction
b	Nt/m/s	Damping coefficient
T	s	Cycle duration
T_s	s	Stance duration
h_{apex}	m	Flight apex position
g	m/s^2	Acceleration of gravity
m	kg	Body mass
J	kg m^2	Body inertia
d	m	Hip joint to COM distance
f	–	As index: front leg
b	–	As index: back leg
g	–	As index: ground variable
e	–	Specific resistance
j	–	Dimensionless inertia
r	–	Relative leg stiffness
p	–	Dimensionless hip separation
Fr	–	Froude number
s	–	Time scale
$*$	–	As superscript: dimensionless

of the robot leg and includes friction modeling, as the sum of Coulomb and viscous friction. The torque delivered at each hip and the force along each robot leg is equal to half the corresponding ones at the virtual leg.

System dynamics are derived using a Lagrangian formulation, with generalized coordinates the Cartesian variables describing the center of mass (COM) position and the main body's attitude. During flight, the robot is under the influence of gravity only. Throughout the stance phase, the robot's toes are fixed on the ground, and act as lossless pivot joints. The dynamics for any phase may be derived from that of the double stance, by removing appropriate terms. Hence, only the double stance dynamics is given, in the form of a set of differential and algebraic equations,

$$m\ddot{x} = -(f_b + k(l_o - l_b) - f_{fr,b})\sin\gamma_b - \tau_b\cos\gamma_b/l_b - (f_f + k(l_o - l_f) - f_{fr,f})\sin\gamma_f - \tau_f\cos\gamma_f/l_f, \tag{1}$$

$$m\ddot{y} = (f_b + k(l_o - l_b) - f_{fr,b})\cos\gamma_b - \tau_b\sin\gamma_b/l_b + (f_f + k(l_o - l_f) - f_{fr,f})\cos\gamma_f - \tau_f\sin\gamma_f/l_f - mg, \tag{2}$$

$$J\ddot{\theta} = \tau_b - d(f_b + k(l_o - l_b) - f_{fr,b})\cos(\gamma_b - \theta) + \tau_f + d(f_f + k(l_o - l_f) - f_{fr,f})\cos(\gamma_f - \theta) + d\tau_b\sin(\gamma_b - \theta)/l_b - d\tau_f\sin(\gamma_f - \theta)/l_f, \tag{3}$$

where

$$\gamma_b = \mathrm{Atan2}(y - d\sin\theta, x_{bt} + d\cos\theta - x),$$
$$\gamma_f = \mathrm{Atan2}(y + d\sin\theta, x_{ft} - d\cos\theta - x), \tag{4}$$

$$l_b = \sqrt{(x_{bt} - x + d\cos\theta)^2 + (d\sin\theta - y)^2},$$

$$l_f = \sqrt{(x_{ft} - x - d\cos\theta)^2 + (d\sin\theta + y)^2}, \tag{5}$$

$$f_{fr,i} = f_c\,\mathrm{sign}(\dot{l}_i) + b\dot{l}_i, \quad i = b, f. \tag{6}$$

3. Dimensional analysis

Dimensional analysis can be applied to all quantitative models and offers an efficient way to display complex data sets. Usually, it makes the subsequent analysis much more useful, because the physical model, as first written, is rather general. The premise of dimensional analysis is that complete equations can be written in a form that is independent of the choice of units, and variables appear in combinations that are dimensionless. Such dimensionless variables are introduced as follows:

$$t^* = \frac{t}{s}, \tag{7}$$

$$x^* = \frac{x}{l_o}, \quad \dot{x}^* = s\frac{\dot{x}}{l_o}, \quad \ddot{x}^* = s^2\frac{\ddot{x}}{l_o}, \tag{8}$$

$$y^* = \frac{y}{l_o}, \quad \dot{y}^* = s\frac{\dot{y}}{l_o}, \quad \ddot{y}^* = s^2\frac{\ddot{y}}{l_o}, \tag{9}$$

$$\theta^* = \theta, \quad \dot{\theta}^* = s\dot{\theta}, \quad \ddot{\theta}^* = s^2\ddot{\theta}, \tag{10}$$

where s is the *time scale* of the system, and the rest of the variables are defined in Table 1.

By substituting (7)–(10) into the equations of motion, given by (1)–(6), one gets a dimensionless description of the system. The resulting motion of the COM can be characterized by two distinct time scales. The first is associated to the inverse of the natural frequency of the vertical oscillation,

$$\frac{s^2k}{m} = 1 \Rightarrow s = \sqrt{\frac{m}{k}}, \tag{11}$$

while the second, to the natural frequency of the horizontal oscillation motion,

$$\frac{s^2g}{l_o} = 1 \Rightarrow s = \sqrt{\frac{l_o}{g}}. \tag{12}$$

Selection of the latter as the time scale of the system, results to a number of dimensionless parameter groups, which are widely used by experimental biologists. These include: (a) the Froude number Fr [12], defined as

$$Fr = \frac{v}{\sqrt{gl_o}}, \tag{13}$$

where v is the robot *forward speed*, (b) the dimensionless inertia j [21], i.e. the robot's body inertia normalized to md^2,

$$j = \frac{J}{md^2} \tag{14}$$

and (c) the leg relative stiffness r [22], that is defined as

$$r = \frac{kl_o}{mg}. \tag{15}$$

For offering this advantage, and because we are primarily interested in the forward motion aspects, the time scale in (12) is chosen to set the equations of motion dimensionless. While the individual dimensionless equations would be different if one uses (11) instead, the relationships between them would be invariant. The following dimensionless parameters are also introduced: (a) dimensionless half hip separation p, defined as,

$$p = \frac{d}{l_o} \tag{16}$$

and (b) the dimensionless viscous friction coefficient b^*, defined as

$$b^* = \frac{b}{m}\sqrt{\frac{l_o}{g}} \text{ or } b^* = 2\zeta\sqrt{r}, \tag{17}$$

where ζ is the damping ratio.

Force and torque variables are finally normalized as

$$f_i^* = \frac{f_i}{mg}, \quad i = b,f,c \quad \text{and} \quad \tau_i^* = \frac{\tau_i}{mgl_o}, \quad i = b,f. \tag{18}$$

The desired dimensionless description of the system results from substituting (7)–(10), (12) and (14)–(18) to (1)–(6) and it is presented next for the double stance,

$$\ddot{x}^* = \left(f_{fr,b}^* - f_b^* - r(1-l_b^*)\right)\sin\gamma_b^* - \tau_b^*/l_b^*\cos\gamma_b^* + \left(f_{fr,f}^* - f_f^* - r\left(1-l_f^*\right)\right)\sin\gamma_f^* - \tau_f^*/l_f^*\cos\gamma_f^*, \tag{19}$$

$$\ddot{y}^* = \left(f_b^* + r(1-l_b^*) - f_{fr,b}^*\right)\cos\gamma_b^* - \tau_b^*/l_b^*\sin\gamma_b^* + \left(f_f^* + r\left(1-l_f^*\right) - f_{fr,f}^*\right)\cos\gamma_f^* - \tau_f^*/l_f^*\sin\gamma_f^* - 1, \tag{20}$$

$$\begin{aligned} pj\ddot{\theta}^* = &-\left(f_b^* + r(1-l_b^*) - f_{fr,b}^*\right)\cos\left(\gamma_b^* - \theta^*\right) + \left(f_f^* + r\left(1-l_f^*\right) - f_{fr,f}^*\right)\cos\left(\gamma_f^* - \theta^*\right) + \tau_b^*/p + \tau_f^*/p \\ &+ \tau_b^*\sin\left(\gamma_b^* - \theta^*\right)/l_b^* - \tau_f^*\sin\left(\gamma_f^* - \theta^*\right)/l_f^*, \end{aligned} \tag{21}$$

where

$$\begin{aligned} \gamma_b^* &= \text{Atan2}\left(y^* - p\sin\theta^*, x_{bt}^* + p\cos\theta^* - x^*\right), \\ amma_f^* &= \text{Atan2}\left(y^* + p\sin\theta^*, x_{ft}^* - p\cos\theta^* - x^*\right), \end{aligned} \tag{22}$$

$$\begin{aligned} b^* &= \sqrt{\left(x_{bt}^* - x^* + p\cos\theta^*\right)^2 + \left(p\sin\theta^* - y^*\right)^2}, \\ f^* &= \sqrt{\left(x_{ft}^* - x^* - p\cos\theta^*\right)^2 + \left(p\sin\theta^* + y^*\right)^2}, \end{aligned} \tag{23}$$

$$fr,i^* = f_c^*\,\text{sign}(\dot{l}_i^*) + b^*\dot{l}_i^*, \quad i = b,f. \tag{24}$$

4. Similarity rules

A similarity rule maintains the constancy of a non-dimensional number. The simplest similarity rule is the geometric similarity. Here, the ratio of any lineal dimension to a characteristic length of the system is constant and all dimensions are magnified by the same factor as compared to a base configuration. For example, if the same materials are used, the mass of a system scales with the cube of the length in geometrically similar systems.

Just as geometric similarity refers to shapes, the concept of dynamic similarity refers to motion. Two motions are said to be dynamically similar if one could be made identical to the other by multiplying all linear dimensions by some constant factor and all time intervals by another. Additionally, dynamic similarity in legged locomotion requires that the Froude numbers of the motions of two quadruped animals (or robots) are equal [12].

According to the dimensional analysis in Section 3 and by observing the dimensionless description of the system, given by (19)–(21), dynamically similar motions require further that the dimensionless parameters in (14)–(16) are equal for motions with the same characteristics, e.g., flight apex, body pitch angle and pitch rate. Repeating for clarity, these parameters, which are connected to robot shape as discussed in Section 1, are: (a) the dimensionless inertia j, (b) the leg relative stiffness r, and (c) the dimensionless half hip separation p, defined in (14)–(16), respectively.

Next, we use an evidential example based on biological data to show similarity requirements. Let the rest leg length be the characteristic scale length. This implies that by doubling the rest length of the leg, the robot is scaled up by a factor of two. Body mass is proportional to the third power of the characteristic length, while the gravitational acceleration does not scale with size. Therefore, in order for the robot to keep moving in a dynamically similar fashion, the leg stiffness should be

quadruplicated, see (15), since the relative stiffness of the leg should be kept constant. This is consistent with biology findings in animal scaling laws [23], where the leg springiness increases with body mass, namely, $k \propto m^{2/3}$.

5. Passive dynamics

It is generally accepted that bounding is essentially a natural mode of the system, and that only minor control and energy effort are required to maintain running. Practically, this motivated us to study the *passive dynamics* of the system. If the system stays close to its passive behavior, then the actuators have less work to do to maintain the motion and energy efficiency is improved. Using passive running, energy savings of 93% are reported in [14].

In this paper, we use a *passive model* that encodes the target behavior of the system and reveals intrinsic system properties and aspects of quadrupedal bounding that may be used as guidelines for the optimal design of quadruped robots. The unactuated and conservative model of our analysis is derived from (19) to (21) by eliminating actuation and energy dissipation terms. It is given here for completeness,

$$\ddot{x}^* = -r(1-l_b^*)\sin\gamma_b^* - r\left(1-l_f^*\right)\sin\gamma_f^*, \tag{25}$$

$$\ddot{y}^* = r(1-l_b^*)\cos\gamma_b^* + r\left(1-l_f^*\right)\cos\gamma_f^* - 1, \tag{26}$$

$$\ddot{\theta} = r\left(\left(1-l_f^*\right)\cos\phi_f^* - (1-l_b^*)\cos\phi_b^*\right)/pj, \tag{27}$$

$$\gamma_b^* = \mathrm{Atan2}\left(y^* - p\sin\theta^*, \ddot{x}_{bt}^* + p\cos\theta^* - x^*\right),$$

$$\gamma_f^* = \mathrm{Atan2}\left(y^* + p\sin\theta^*, x_{ft}^* - p\cos\theta^* - x^*\right), \tag{28}$$

$$\gamma_b^* = \theta^* + \phi_b^*,$$

$$\gamma_f^* = \theta^* + \phi_f^*, \tag{29}$$

$$l_b^* = \sqrt{\left(x_{bt}^* - x^* + p\cos\theta^*\right)^2 + \left(p\sin\theta^* - y^*\right)^2},$$

$$l_f^* = \sqrt{\left(x_{ft}^* - x^* - p\cos\theta^*\right)^2 + \left(p\sin\theta^* + y^*\right)^2}. \tag{30}$$

In order to evaluate the performance of the above model, we focus on system *periodic steady state trajectories*, which are identical trajectories that repeat themselves during locomotion. Following a similar procedure as in [3,8], we employ a *Poincaré Map* technique to formulate these trajectories. The return map connects the system state at a well-defined locomotion event to the state of the same event at the next cycle. Here, this event is chosen to be the apex height, because the vertical velocity is always zero there. Furthermore, the distance traveled has no influence on the locomotion cycle. Thus, the state vector $\mathbf{x}^*$ at apex height consists of the apex height y^*, the body pitch angle θ^*, the forward speed $\dot{x}^*$, and the body pitch rate $\dot{\theta}^*$ only, i.e.,

$$\mathbf{x}^* = \begin{bmatrix} y^* & \theta^* & \dot{x}^* & \dot{\theta}^* \end{bmatrix}. \tag{31}$$

The state vector at apex height for some cycle n, $\mathbf{x}_n^*$, constitutes the initial conditions. Based on these, the flight equations, derived from (25) to (27) by removing terms not permanent to the phase, are integrated until one of the touchdown events occurs, e.g., front or back leg stance (see Fig. 2 top and middle). The touchdown event triggers the next phase, whose dynamics are integrated using as initial conditions the final conditions of the previous state. Depending on system configuration,

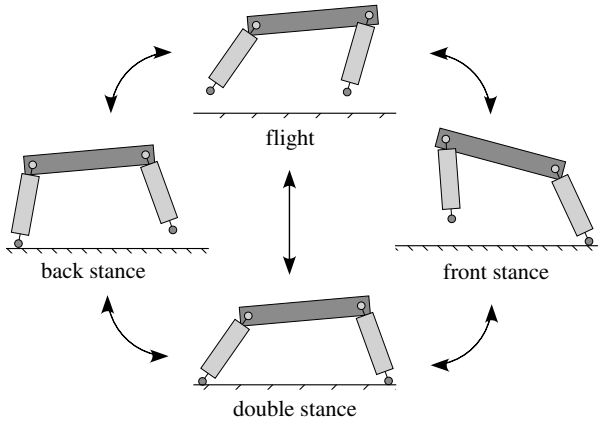

Fig. 2. Bounding with the front or back leg stance touchdown event (right and left), bounding with the double stance, i.e. pronking (bottom), and the flight phase.

the next phase could be either flight, i.e., bounding without double stance, or double stance. Pronking is the case of bounding with zero body pitch rate, and the touchdown event following flight is the double stance, which is in turn followed by flight, i.e. there is no back or front leg stance phase (see Fig. 2 bottom).

Successive forward integration of the dynamic equations of all the phases yields the state vector at apex height of the next stride, which is the value of the *Poincaré* return map **F**. If the state vector at the new apex height is identical to the initial one, the cycle is repetitive and it is yields a *fixed point*. Mathematically, this is given as

$$\mathbf{x}^*_{n+1} = \mathbf{F}(\mathbf{x}^*_n). \tag{32}$$

It must be noted that existence of such fixed points seems to be the rule, rather than the exception.

In order to determine the conditions required to result in steady state cyclic motions, we resort to a numerical evaluation of the return map using a *Newton–Raphson* method. By employing this method, a large number of fixed points can be found for different initial conditions and different touchdown angles. These angles, although they are not part of the state vector $\mathbf{x}^*_n$, and are not generalized coordinates, they directly affect the value of the return map as they determine touchdown and liftoff events and impose constraints on the motion of robot during back/front leg and double stance phases.

Variant combinations of robot's dimensionless parameters, as defined in (14)–(16), also result to different fixed points. These design parameters vary between their extreme values found either in experimental biology references [23,24], or are imposed by common sense. Particularly, they range as follows,

$$j = 0.70\text{—}1.45, \quad r = 10\text{—}30, \quad p = 0.25\text{—}1.00. \tag{33}$$

6. Energetic cost of locomotion

Following the previous analysis and assumptions, the robot executes a passive motion according to the sets of initial conditions found by employing the above-mentioned method. Then, no energy is lost or added to the system. This may sound unrealistic, but if one uses actuators *just* to compensate for the energy lost, and initial conditions that yield a passive trajectory, then the robot will execute an active gait very close to the passive gait and the system can be studied using (25)–(30), as in the lossless case.

Then, the only energy required to sustain the motion is the amount dissipated over one stride, E, which is the sum of the mechanical energy E_{m} dissipated due to friction at legs, the kinetic energy lost in ground damping and compression at touchdown, E_{g}, and the electrical losses due to ohmic resistances at the motors, E_{el},

$$E = E_{\mathrm{m}} + E_{\mathrm{g}} + E_{\mathrm{el}}. \tag{34}$$

The dimensionless mechanical energy losses, E^*_{m}, due to leg friction are found using (35) to be

$$E^*_{\mathrm{m}} = f^*_c T_s + b^* \left(\int_0^{T_{sb}} \dot{l}^{*2}_b \mathrm{d}t^* + \int_0^{T_{sf}} \dot{l}^{*2}_f \mathrm{d}t^* \right). \tag{35}$$

In addition to friction losses, energy losses due to the interaction of robot's legs with the ground exist. Particularly, the running robot dissipates some of its kinetic energy in ground damping and compression at touchdown. Note here that ground is considered even and that we assume no slip during contact. Ground surface is modelled as a parallel spring-damper system that influences the robot only when the feet are in contact with the ground, i.e., when the vertical velocity is negative. The acting direction of ground spring-damper system is *along* the direction of robot's interacting leg. Each time a foot touches the ground, the rest position of the ground spring is reset to the point at which the foot first touches. The coefficient of friction between each foot and the ground is assumed to large, so that slipping never occurs. Finally, for a wide yet reasonable range of damping and stiffness coefficients, the ground displacement (deformation) is negligible compared to leg length, and the integrated robot and ground motion equations can be approximated by (25)–(30) and (36),

$$b^*_{\mathrm{g}} \dot{l}^*_{\mathrm{g},i} + r_{\mathrm{g}} l^*_{\mathrm{g},i} = r(l^*_i - 1), \quad i = b, f, \tag{36}$$

while the ratio of dimensionless ground damping to spring coefficient is the dimensionless ground time constant

$$\tau^*_{\mathrm{g}} = \frac{b^*_{\mathrm{g}}}{r_{\mathrm{g}}}. \tag{37}$$

To this end, the dimensionless ground energy losses, E^*_{g}, due to ground damping and ground permanent deformation for each leg are found using (38) to be,

$$E^*_{\mathrm{g},i} = \int_0^{T_{s,i}} \left(b^*_{\mathrm{g}} \dot{l}^*_{\mathrm{g},i} + r_{\mathrm{g}} l^*_{\mathrm{g},i} \right) \dot{l}^*_{\mathrm{g},i} \mathrm{d}t^*, \quad i = b, f. \tag{38}$$

Electrical losses due to motor ohmic resistance also exist, but their effect is lumped to the effort required by the actuators to sustain the motion and is comprehensively discussed later.

In our analysis, distance covered is of the major consideration, and thus the energy cost for moving a unit distance is considered. The rate of dissipated energy per unit time is the required power P to sustain the passive motion over one cycle, and the rate of distance covered per unit time is the forward speed of locomotion v. If the power cost for moving with unit speed is further normalized to robot weight mg, dimensionless criterion, the *specific resistance* e, [25], yields as

$$e = \frac{P}{mgv}. \tag{39}$$

The specific resistance is a good overall criterion that can be used for optimized robot designs. Therefore, robot parameters and/or motion variables should be chosen so that the criterion in (39) is minimized.

It is has been shown that passive running is the most efficient type. Nevertheless, depending on the initial conditions, the characteristics of a passive gait, such as the stance duration and the energy dissipated, will vary. To analyze this effect in the dimensionless framework, i.e., using dimensionless parameters, so as to reveal the effect of scaling in determining robot physical parameters, we define a variation of e, the dimensionless *cost of locomotion* e^*, as,

$$e^* = \frac{P^*}{v^*} = \frac{E^*}{T^*}\frac{2p}{Fr}, \tag{40}$$

where P^* is the dimensionless required mean power to sustain the passive motion over one cycle or alternatively the dimensionless energy dissipated over one stride E^* divided by cycle duration T^*, and v^* the dimensionless forward speed of the robot, defined as the Froude number Fr normalized to the dimensionless body length, which is approximated with double the dimensionless half hip separation, p. Our work shows that e^* varies for different gaits, and that the differences are considerable. Hence, it is necessary to evaluate the effect of each dimensionless parameter and/or of their combinations to e^* and identify the set of parameters, for which the criterion in (40) is least.

If an optimal set of robot parameters has been chosen for a given set of initial conditions and ground surface properties, and if, say, ground properties change, then these parameters may require adjustment to maintain optimality. This is consistent with the behavior of animals, which adjust leg stiffness for running efficiently on various ground surfaces or at various speeds [26]. Therefore, a range of ground stiffness and damping properties are going to be used, so as to determine their effect on the cost of locomotion, given by (40).

7. Parametric study

In this section, the results of the parametric analysis are presented and design guidelines are proposed. The results are obtained by simulation and for a parametric range of robot physical parameters, motion characteristics and ground surface properties. In each figure, the cost of locomotion given by (40), is plotted against two of the dimensionless parameters. The *filled* (white) *stars* denote the optimal value of the variable that lies in the horizontal axis for a given value of the variable in the vertical axis, while the *hollow* (*black*) *stars* represent the global minimum of the criterion, i.e. a combination of robot physical parameters or motion characteristics or ground surface properties, for which the performance is superior and there-

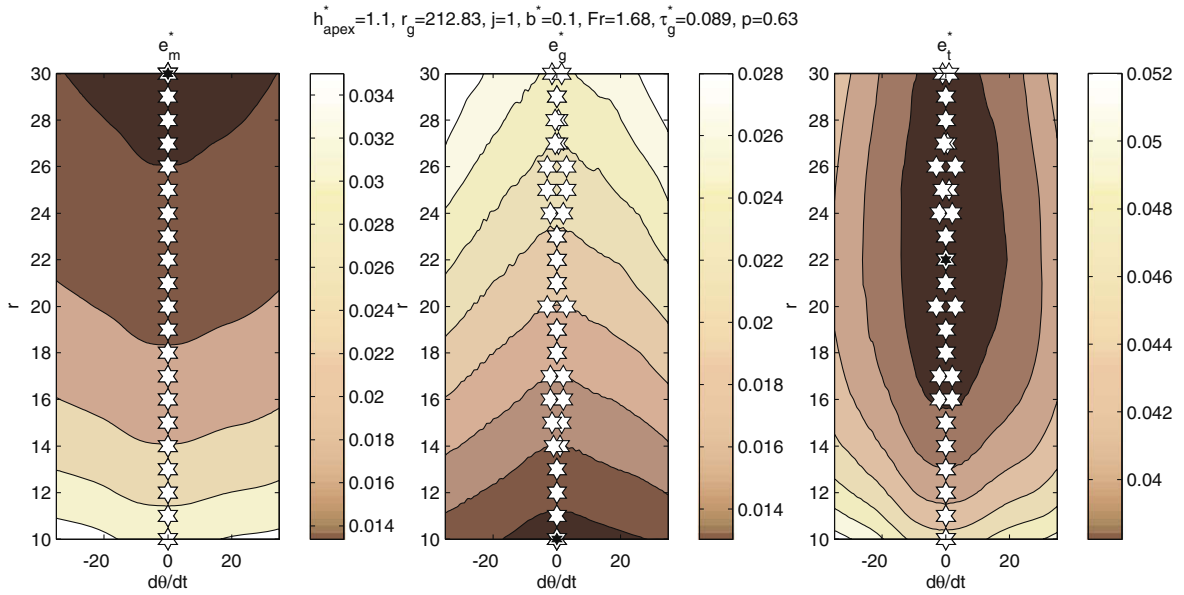

Fig. 3. The effect of relative stiffness and pitch rate on mechanical (right), ground (middle) and overall (right) specific resistance.

fore leads to a *design guideline*. Each time, the "non-participating" parameters are fairly changed so as to show that the results are not limited to a certain parametric range. For convenience, their value is given at the title of each figure.

The effect of *relative stiffness* and *pitch rate* on dimensionless specific resistance (DSR) is shown in Fig. 3. As shown, the effect of relative stiffness on mechanical (left) and ground (middle) specific resistance is competitive. The mechanical DSR (MDSR) is reduced for larger values of the relative stiffness, while the ground DSR, (GDSR), is minimized for the smallest one. One may achieve a large relative stiffness, see (15), by increasing either the leg spring stiffness or the leg rest length, or by reducing the body mass of the robot. For example, usage of soft springs will cause more leg compression compared to harder ones resulting to excessive energy dissipation due to friction. But, the resulting forces that interact with the ground will be much smaller than the ones produced by harder leg springs and will generally result to reduced energy dissipation due to ground damping and compression. Also, by increasing leg length or making the body mass lighter, and so increasing relative leg stiffness, smaller touchdown angles are required for the robot to sustain its motion, which generally leads to smaller energy dissipation in legs. On the other hand, hitting the ground with smaller touchdown angles leads to greater energy dissipation since the component of the leg force normal to ground surface is larger. Therefore, it can be seen, that there exists a competitive effect between MDSR and GDSR, which ensures the existence of an optimal relative stiffness that minimizes the cost of locomotion, (40), as illustrated in Fig. 3 (right). This leads to our first finding.

Finding 1. There is a particular value of leg relative stiffness that is optimal in terms of locomotion cost, which lies in between the extreme values of leg relative stiffness that are found in experimental biology references [23,24].

In Fig. 3, it is also evident that MDSR (left) and GDSR (middle) is a convex and concave function of pitch rate, respectively, for given relative stiffness. This indicates that the optimal pitch rate is zero, as shown in Fig. 3 (right) and thus, the most economical type of motion is for the case when the back and front *leg pairs* are *in phase*, i.e., for the pronking gait.

Finding 2. Pitching motion should be kept to a minimum, for the robot to move most efficiently all the time.

However, the optimal value of leg stiffness should be adjusted to ground stiffness for robot efficient motion. This is concluded from Fig. 4, where the effect of leg and ground relative stiffness on overall specific resistance is plotted for the pronking gait. Their function is linear, implying that one should not search for an optimal value of relative stiffness, but rather one should determine the optimal leg to ground stiffness *ratio*. This is also supported by experimental biology findings, as animals adjust their leg stiffness for efficient running on different ground surfaces [26]. The shape of the *geometric locus*, along which the optimal set of leg and ground stiffness are moving, heavily depends on the dimensional viscous friction coefficient, as illustrated in Fig. 5. Since ground losses are independent of leg friction, while mechanical losses are proportional to the viscous friction coefficient, see (35), the optimal leg to ground stiffness ratio set is moving to the right or left when b^* increases or decreases, respectively.

Finding 3. Leg stiffness should be adjusted to ground stiffness for the robot to run economically on different ground surfaces.

Guideline 1. For a given robot structure, known ground surface properties and specific motion characteristics the optimal leg spring stiffness can be found from Figs. 3 and 4, in a consecutive manner.

Moving on, for every value of leg relative stiffness an optimal forward speed exists. This is indicated in Fig. 6, where the effect of *relative stiffness* and *Froude number* on overall specific resistance is drawn. Specifically, the optimal running speeds

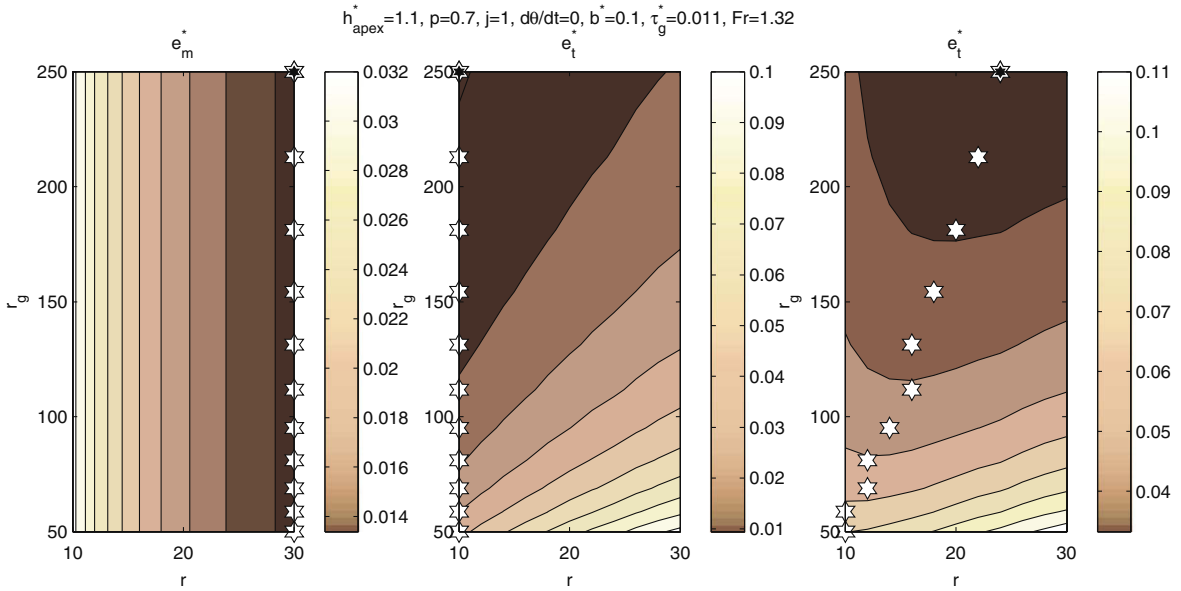

Fig. 4. The effect of leg and ground relative stiffness on mechanical (right), ground (middle) and overall (right) specific resistance.

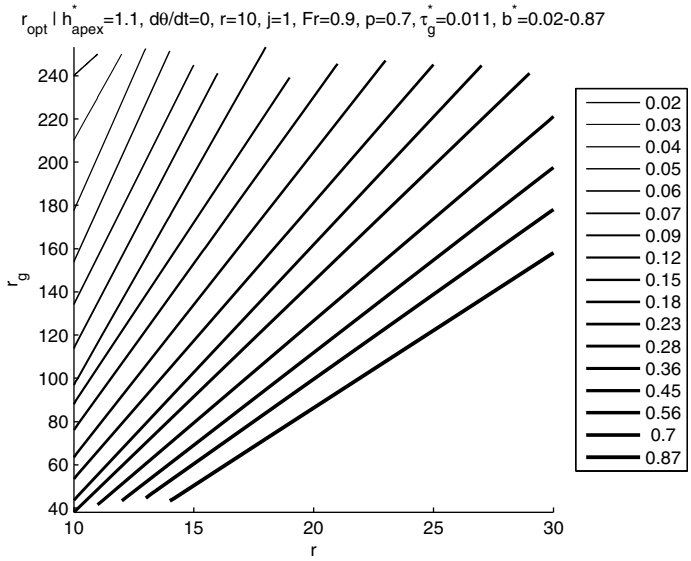

Fig. 5. The effect of dimensional viscous friction coefficient on the shape of the *geometric locus*, along which the optimal set of leg and ground stiffness is moving.

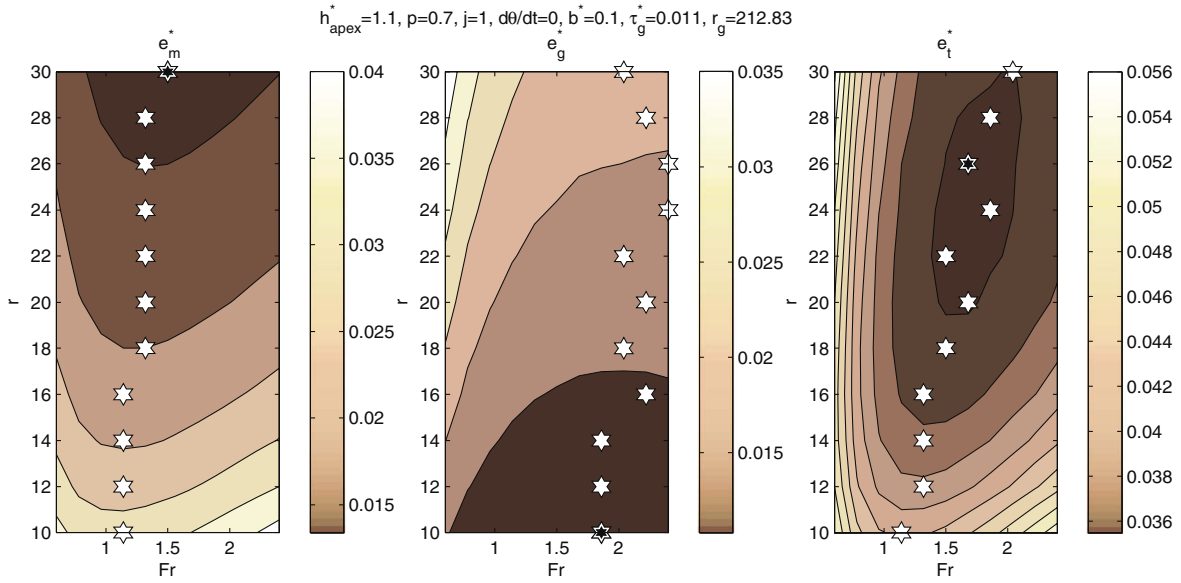

Fig. 6. The effect of relative stiffness and Froude number on mechanical (right), ground (middle) and overall (right) specific resistance.

of the quadruped lie along a steep line for a wide range of relative stiffness values. This fact imposes that the robot could be designed for a *nominal forward speed*, as selected with the aid of Fig. 6, and operated close to its economical function for a sufficient variation of forward speeds. One may also notice that the range of optimal forward speed is between 1.5 and 2.4. In this range lies the Froude number that corresponds to the preferred bounding speed of many quadrupeds [26]. Outside this range, these animals prefer to walk (for slower speeds) or gallop (for higher speeds).

The existence of an optimal forward speed for given robot configuration and ground surface properties is also consistent with [27]. Although a one legged robot is studied in [27], the dynamics of the *pronking* quadruped is similar to those of one-leg hopper. In the end [27] concludes that there exists a particular passive gait, of all those possible, i.e., an optimal touch-down angle, that leads to the least dissipated energy per meter of travel. This optimal touchdown angle results to a particular (optimal) forward speed.

Finding 4. There exists an optimal speed to run efficiently for a given robot configuration and ground surface properties, which is neither very slow nor fast.

Guideline 2. The robot could be designed for a *nominal forward speed* with the aid of Fig. 6, and operated close to its efficient function for a sufficient range of forward speeds.

In Fig. 7, the effect of dimensionless half *hip separation* and *pitch rate* on MDSR (left), GDSR (middle) and overall (right) specific resistance is presented. Forward speed is *normalized* to body length, according to (40). At this point, we assume without loss of generality, that body length is approximately the distance between the two hips of the robot. Two, rather obvious, conclusions are drawn from Fig. 7. Firstly, the optimal pitch rate for a given dimensionless body length is zero. This strengthens the conclusion drawn preciously from Fig. 3 (right), that *pronking* is the most efficient gait for a bounding robot, and that pitching motion should be kept in minimum for efficient running (see also Finding 2). Secondly, each of the mechanical, ground and overall specific resistances exhibit a global minimum value, which corresponds to different values of the dimensionless half hip separation though.

Explicating, the dimensionless hip separation may change by changing either leg rest length or body length, see (16). Recall at this point that the forward speed of the robot is normalized to body length, and thus by increasing leg length, both the dimensionless body length and the Froude number are reduced proportionally, so as to keep the reference dimensionless forward speed constant, see (40). Broadly speaking, more effort is needed to move with greater speed, but given the fact the cost of locomotion is normalized to forward speed, it is concluded that moderate forward speeds are preferable, and that neither very long nor short body lengths should be considered during the robot design phase. On the other, by increasing leg length the relative leg stiffness is so increased and smaller touchdown angles are required for the robot to sustain its motion, as discussed earlier. Generally this leads to smaller energy dissipation in legs and greater energy dissipation in ground.

Finding 5. There is a particular value of the dimensionless body length that is optimal in terms of locomotion cost, which is neither very large nor small.

This tradeoff is evident in Fig. 7, where the larger the leg relative stiffness is the greater its effect on MDSR is, compared to the effect of the dimensionless body length. Therefore, the optimal value of the dimensionless half *hip separation*, p, that minimizes the cost of locomotion, see Fig. 7 (right), depends heavily on the *relative stiffness*, r, as well as on the *optimal ratio* between p and r, which keeps the overall specific resistance minimal. This ratio, should be considered first and can be found using Fig. 8, where MDSR (right), GDSR (middle) and overall (right) specific resistance with respect to p and r are plotted.

According to Fig. 6, large values of relative stiffness result to small MDSR. Contrarily, GDSR is reduced for small values of the relative stiffness. Furthermore, for given relative stiffness, the MDSR and GDSR is rather a convex and concave function of the dimensionless half hip separation, respectively, due to the fact that the cost of locomotion is normalized to the forward speed, as mentioned earlier. With the aid of Fig. 8, the optimal dimensionless body length may be determined for given motion characteristics and known ground properties, provided that the optimal relative stiffness has been selected earlier with the aid of Figs. 3 and 4, as described previously.

Finding 6. There exists an optimal relative leg stiffness and dimensionless body length ratio for given motion characteristics and ground surface properties.

Guideline 3.The optimal dimensionless body length may be determined for given motion characteristics and known ground surface properties from Fig. 8, provided that the optimal relative stiffness has been selected earlier as in Guideline 1.

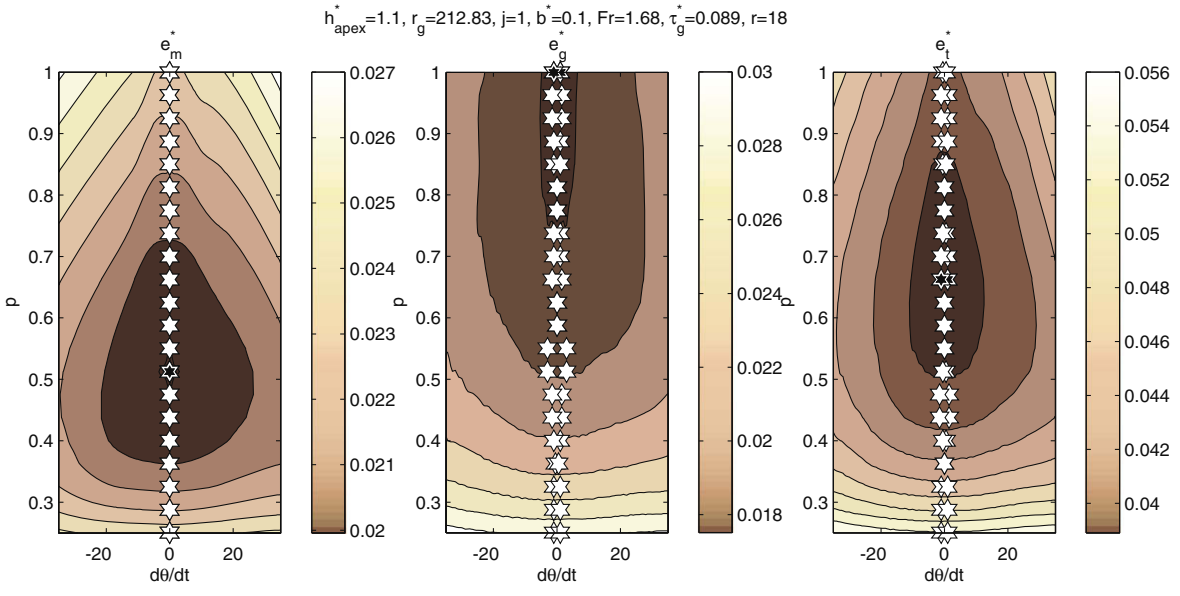

Fig. 7. The effect of dimensionless body length and pitch rate on mechanical (right), ground (middle) and overall (right) specific resistance.

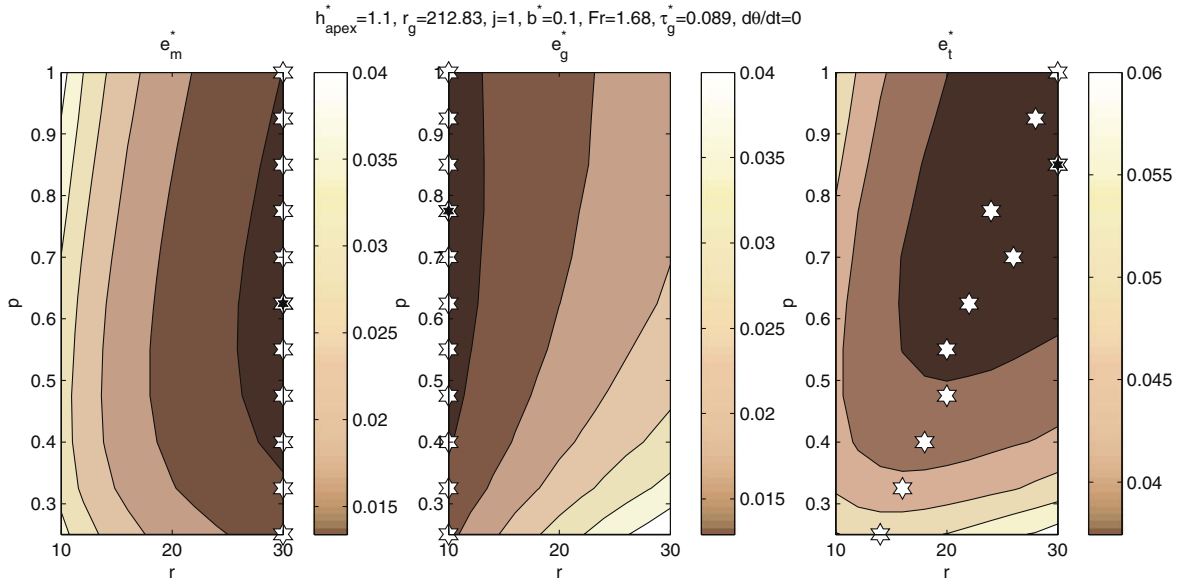

Fig. 8. The effect of dimensionless stiffness and body length on mechanical (right), ground (middle) and overall (right) specific resistance.

Finally, the effect of *dimensionless inertia* and *pitch rate* on overall specific resistance is presented in Fig. 9. Their effect is rather complex, and thus difficult to derive particular design guidelines from. Specifically, for large, either negative or positive pitch rates, the overall specific resistance is reduced when the dimensionless inertia decreases. On the contrary, for the pronking gait, the overall specific resistance is almost constant up to unit dimensionless body inertia j, while for even larger values, the overall specific resistance is reduced. Surprisingly, the global minimum values are found for small pitch rates, i.e. approximately 7.5 (in absolute value), and for the largest value of the dimensionless inertia ($j = 1.45$). It is noted here, that dimensionless inertias larger than 1 are rarely found in nature. On the other hand, it is simple for a robot to attain a specific value of dimensionless inertia by proper hip placement or body mass redistribution. Nevertheless, the effect of the dimensionless inertia is not significant to the value of overall specific resistance, for small pitch rates, so other criteria should guide the designer to select its value, such as motion stability, control aspects and/or design simplifications.

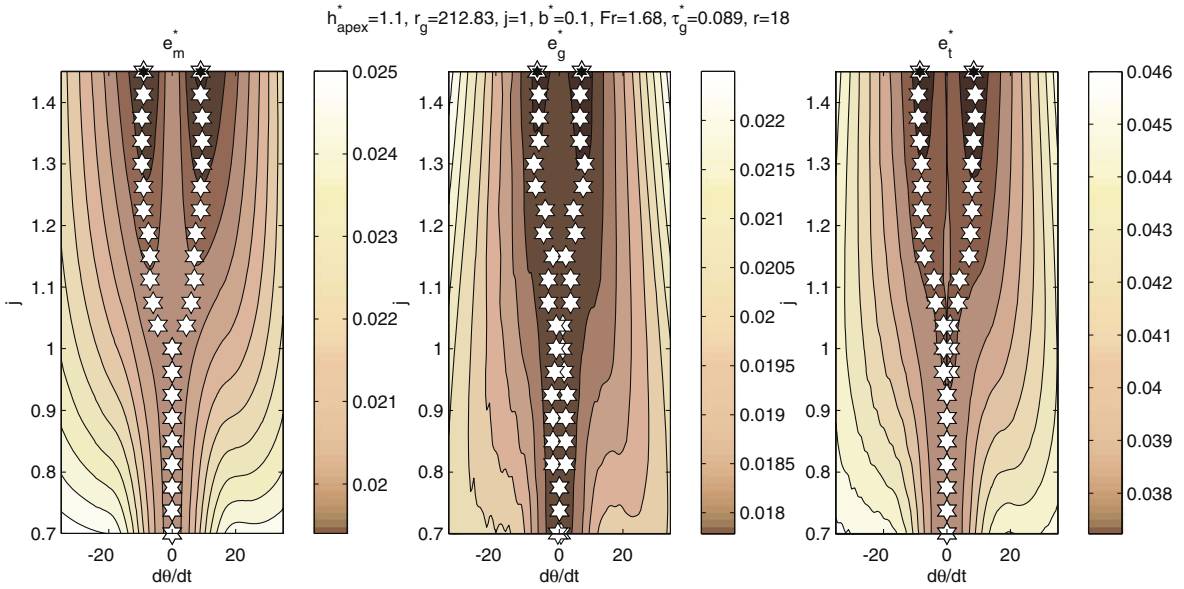

Fig. 9. The effect of dimensionless inertia and pitch rate on mechanical (right), ground (middle) and overall (right) specific resistance.

8. Electric scaling laws

The techniques for developing scaling laws for electromagnetic subsystems are derived and analyzed here. Specific scaling laws are developed and verified using data from commercial systems. Finally, applications of the scaling laws that can provide direction in quadruped robot design are discussed. The laws developed focus on the variation of the property of interest with respect to the scale factor, i.e., the characteristic length. Here, the motor *characteristic length*, s_m, is defined as the cube root of the motor volume and has units of m (see Table 2). Another size scale factor, defined as the product of the motor characteristic length, motor's weight and gravity acceleration and has units of N/m (see Table 3), could be used, too. While the individual scaling laws would be different, the relationships between scaling laws would be invariant.

Initially, simple scaling laws are derived from first principles, where the basis for these laws is obvious. More complex and less intuitive laws may be produced by combining these simple scaling laws with each other and with engineering relationships. Laws are expressed as an exponent of the characteristic length. All scaling laws presented here are, by their nature simple, and applicability over a wide range may be limited. It is important to remember that these laws are intended to provide guidance and intuition into quadruped robot design, but are not meant as a substitute of a more detailed analysis.

8.1. Electric motors

Most macroscopic electric motors rely on magnetic fields produced by electric currents or permanent magnets. As shown in Table 2, where the electric motor scaling laws are summarized, the magnetic field produced by magnets is invariant with scale. In a DC electric motor, forces on moving conductors generate the motor output torque. The force on a single still, current carrying, conductor is a second order (with respect to scale) law. Motor stall torque is the product of such forces acting on multiple conductors that linearly increase in number with scale and rotor radius, and thus it is a fourth order law (see Table 2, where the rationalization for the derived electric motor scaling laws is given in detail).

Empirical evidence for these scaling laws is easily found. For example, consider the fourth order torque scaling law. Fig. 10 illustrates the relationship of motor size vs. stall torque, for a series of commercially available permanent magnet DC motors [28]. The motor scale length here is defined as the cube root of motor volume, as defined earlier and presented in Table 2. The correlation between "actual" and "prediction" values using the fourth order scaling law is very strong.

Table 2
Electric motor scale laws

Name	Formula	Order	Variables
Area	$A \propto l^2$	2	l – Characteristic length (1)
Mass	$M \propto (\rho, l^3)$	3	ρ – Material density (0)
Armature resistance	$R_a = \frac{1}{c_w}\frac{l_w}{\pi r_w^2}$	−1	c_w – Wire conductivity (0) l_w – Wire total length (1) r_w – Wire diameter (1)
Magnetic force on (still) conductor	$F = Bl_r\frac{V_a}{R_a}$	2	B – Magnetic field (0) l_r – Rotor length (1) V_a - Armature voltage (0)
Motor (stall) torque	$\tau_m = N_c Bl_r\frac{V_a}{R_a}r_r$	4	r_r – Rotor radius (1) N_c – Number of conductors (1)
Stress-induced speed limit	$\omega = \frac{1}{r}\sqrt{\frac{8\sigma}{(3+\nu)\rho}}$	−1	ν – Poisson's ratio (0) σ – Allowable stress (0) r – Disk radius (1)
Gearing load factor	$K_v = \frac{C}{C+V_m^{0.5}}$	−0.5	V_m – Pitch-line speed (1) C – Constant (0)
Motor characteristic length (scale)	$s_m = \sqrt[3]{\pi r_m^2 l_m}$	1	r_m – Motor radius (1) l_m – Motor length (1)

Table 3
Brushless DC Servomotors [28] scaling factors

Variable (=f)	Factor (=C)	Value	Units	Function
No-load speed vs. scale s_m ($s_m = \sqrt[3]{\pi r_m^2 l_m}$)	ω_o^*	316.9	–	$f(s_m) = C\cdot(g/s_m)^{1/2}$
Max. permissible speed vs. scale	ω_g^*	75.20	–	$f(s_m) = C\cdot(g/s_m)^{1/2}$
Stall torque vs. size (=$m_m g\ s_m$)	τ_{stall}^*	33.00	–	$f(s_m) = C\cdot(m_m g\ s_m)^1$
Max. permissible torque vs. size	τ_{max}^*	5.300	–	$f(s_m) = C\cdot(m_m g\ s_m)^1$
Motor equivalent density vs. scale	ρ_m	5.282×10^3	kg/m^3	$f(s_m) = C\cdot s_m^0$
Reduction vs. No. of stages (=N)	C_1	1.400	–	$f(N) = 1\cdot e^{C\cdot N}$
Efficiency vs. No. of stages (%)	C_2	10.00×10^{-3}	–	$f(N) = 100\cdot e^{-C\cdot N}$

8.2. Planetary gearheads

In most instances, electric motors run at far higher speeds and lower torques than those required for quadruped robot joints. Therefore, gearboxes must be used to match motor speed and torque to its load, i.e. the hip/leg assembly. The diverse configurations and mechanics of gearboxes, as well as brevity requirements, preclude a detailed discussion of the scaling of gearboxes here. However, since speed is inversely proportional to motor size as indicated in Table 2, scaling down can result at very high motor speeds requiring large speed reduction ratios.

Additionally, the load transmitted through the gearbox depends heavily on the gear quality. To take care of this, manufacturers employ a dynamic load factor. For precision gears, the strength of the gear tooth depends, among other factors, on the square root of surface speed, which is often also referred to as pitch-line speed. Therefore, the load factor is an inverse square root order law of motor size (see Table 2). This is also evident empirically from Fig. 11, which displays motor size vs.

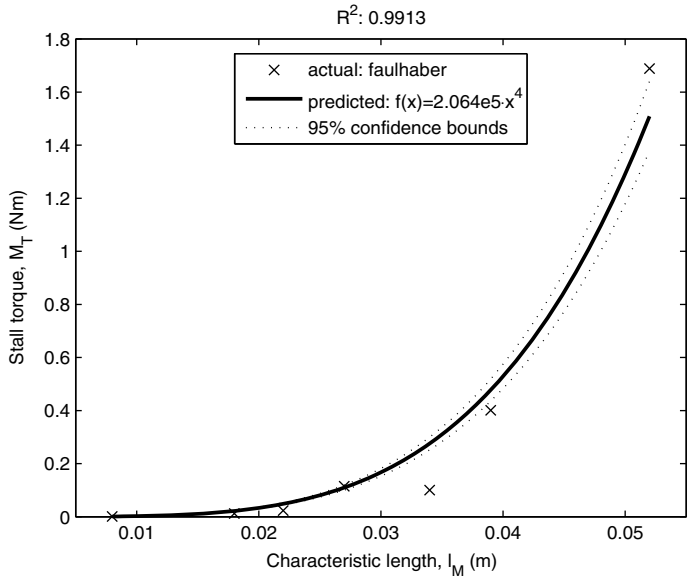

Fig. 10. Motor size vs. stall torque for a series of commercially available permanent magnet DC motors [28].

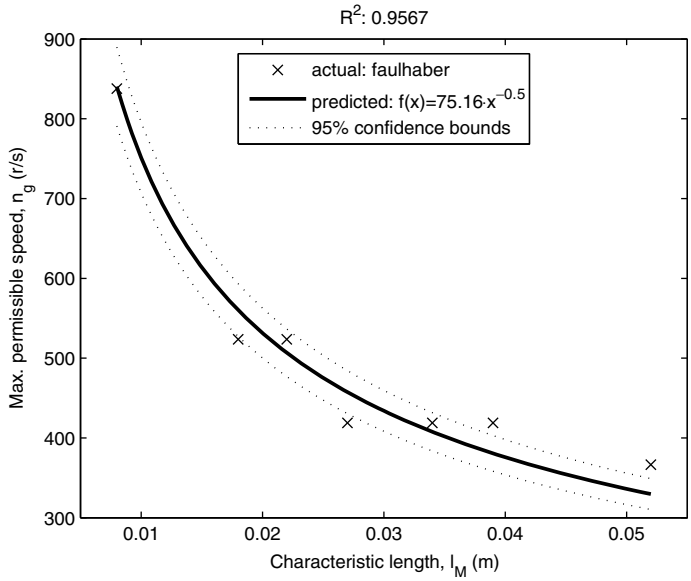

Fig. 11. Motor size vs. max. permissible speed for a series of commercially available precision planetary gearheads [28].

maximum permissible speed for a series of commercially available precision planetary gearheads, with gearbox data taken from [28].

Practical reduction ratios achievable by any type of planetary gearheads are limited in range. Furthermore, high ratios mean multiple reduction stages. The number of stages of speed reduction is a concern not only because of the relative bulk, weight and complexity of multi-stage reducers, but also because efficiency degrades exponentially with the number of reduction stages.

9. Motor effect study

Following the previous observations, the robot executes an active gait very close to the passive motion according to the sets of initial conditions found by employing the *Poincaré* Map technique, which favors its natural dynamics. As explained earlier, in this case the passive dynamics can be used to describe system motion. The amount of energy injected into the system by the motors, which are controlled to exert a desired constant torque. This torque τ^* is given, in its dimensionless form, as

$$\tau^* = \frac{\tau}{mgl_o}. \tag{41}$$

The dimensionless angular velocity about the hip ω^*, is given as

$$\omega^* = \omega\sqrt{\frac{l_o}{g}}. \tag{42}$$

Generally speaking, in work cycles, all operating points must lie beneath the motor torque-speed characteristic curve drawn for the maximum drive voltage. Mathematically, this means that the for all operating points (ω, τ), the following must apply,

$$1 > \frac{\omega}{\omega_o} + \frac{\tau}{\tau_{\text{stall}}}, \tag{43}$$

where ω_o is the no-load speed, and τ_{stall} is the motor stall torque. Apparently, the performance of the electric drive is limited by other factors, too. Of those, the most important ones include the maximum permissible speed at the input of the gearbox and the maximum permissible continuous torque delivered due to thermal considerations.

According to the dimensional analysis discussed in Section 3 and the electric scaling laws presented in Table 2, motor stall torque τ_{stall} and no-load speed ω_o in (43) can be scaled as

$$\tau_{\text{stall}} = \tau^*_{\text{stall}} m_{\text{m}} g s_{\text{m}}, \tag{44}$$

$$\omega_o = \omega^*_o \sqrt{\frac{g}{s_{\text{m}}}} \tag{45}$$

since motor mass m_{m} scales with the cubic power. The rest of the associated indices and variables are defined in Tables 1 and 2.

By substituting Eqs. (41), (42), (44) and (44) in (43), a non-dimensional form of the motor–load curve, i.e. a universal motor–load curve, results and is given by

$$\frac{l_o^{-0.5} i_{\text{g}} \omega^*}{l_{\text{m}}^{-0.5} \omega^*_o} + \frac{m l_o \tau^*}{m_{\text{m}} s_{\text{m}} \tau^*_{\text{stall}} i_{\text{m}} n_{\text{m}}} < 1, \tag{46}$$

where i_{g} is the reduction ratio and n_{g} is the efficiency of the gearbox. This universal motor–load curve drawn here, see Fig. 12, refers solely to the electric drives selected for this study [28]. However, the methodology for constructing such a curve is not restricted to these, but could apply to all electrically driven systems, and also could have been derived from data from different motor vendors.

In non-dimensional work cycles, all operating points must lie beneath the universal curve at a maximum voltage. The motor scaling factors, on the basis of which the universal curve is drawn, depend on the existing range of commercially available permanent magnet DC motors given in [28]. Their range of products is finite due to technology limitations and economic restraints, for example, in larger scales, it may be much more cost effective to use other electric actuation technologies, or in the micro-scale, it is necessary to use actuators operating on entirely other principles. For the purposes of the current work, we use the scaling factors presented in Table 3, which are derived from scaling the brushless DC electric drives from [28] based on the analysis presented in Section 8.

The *length ratio L*, i.e. the ratio of leg length to motor characteristic length, and the *mass ratio M*, i.e. the ratio of robot mass to motor mass, that appear in (46), reflect the proportion between the size of the robot and the motor(s). In this sense, by comparing the length or mass ratios of various robots for a given motor size, a larger length ratio means that the size of the robot is relatively larger, and a larger mass ratio means that the robot is capable of carrying a bigger payload, if the structural mass is kept constant. Likewise, for given robot size, a larger mass ratio implies that the size of the actuator needed to propel the robot and the desired payload is relatively smaller.

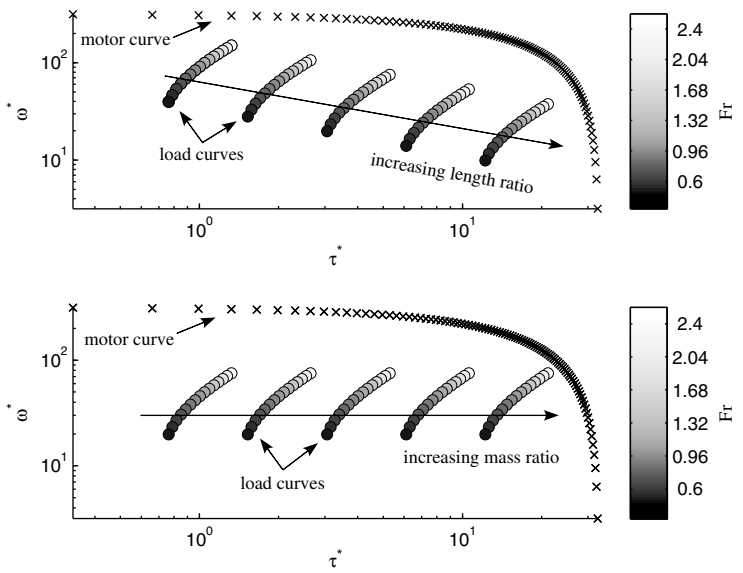

Fig. 12. The universal motor curve and dimensionless load curves for various combinations of length (upper) and mass ratio (lower).

Fig. 12 displays the universal motor curve along with various load curves, drawn by simulating an active gait, very close to the passive one, for the bounding quadruped described by (25)–(30), for increasing length (upper) and mass (lower) ratios. The Froude number, which is defined earlier, and is repeated here for completeness,

$$Fr = \frac{\dot{x}}{\sqrt{g l_o}} \tag{47}$$

varies from 0.6 to 2.4, according to the limits that correspond to the extreme bounding speeds found in nature [12]. The rest of the dimensionless design parameters are kept constant and they are given in the title of each figure. Each marker on the load curves corresponds to the maximum required speed and torque in a passive bounding cycle with zero pitch rate, i.e. pronking, while the background color of the marker corresponds to the value of the Froude number, which is also quantified at the colorbar next to the each subplot.

Since the mass of a system is typically scaled up with a third order law with respect to the characteristic length (see Table 2), the separate length and mass ratios could be reduced to a single ratio using the corresponding densities, namely motor and robot equivalent densities. The *motor equivalent density*, ρ_{m}, is derived from motor data (10 different sized Brushless DC Servomotors [28]) using the scaling function presented in Table 3, while *robot equivalent density*, ρ, is estimated by a series of biological data extracted from various experimental biology works. Fig. 13 presents the leg length, which is the typical scale factor for living and artificial quadrupeds, vs. body mass for a series of quadruped animals, from small rats to large horses. Using the best fit shown in Fig. 13, ρ is found to be 224.2 kg/m^3.

In the same figure, we have added data from existing legged robots, such as Scout-II [3], BigDog [4], PAW [5], Tekken [6] and RHex [17]. Surprisingly, legged robot data also fits satisfactorily the same third order scaling law, with the same density ρ. Therefore, in the analysis to follow, we employ the density value of 224.2 kg/m^3. We note here though that even if one uses a different value for this density, the proposed methodology is still valid and can be applied to yield optimal designs.

Since the overall robot mass m is of significant importance for most applications, the value of the *mass*ratio M can be obtained by dividing the target robot mass with the motor mass m_{m},

$$M = \frac{m}{m_{\mathrm{m}}}. \tag{48}$$

By substituting the mass ratio with the third order scaling law with respect to the characteristic length and the equivalent motor and robot densities in (48), one gets,

$$\frac{m}{m_{\mathrm{m}}} = \frac{\rho l_o^3}{\rho_{\mathrm{m}} s_{\mathrm{m}}^3}. \tag{49}$$

From (49), the *length ratio* L can be calculated as

$$L = \frac{l_o}{s_{\mathrm{m}}} = \sqrt[3]{\frac{\rho_{\mathrm{m}}}{\rho} M}. \tag{50}$$

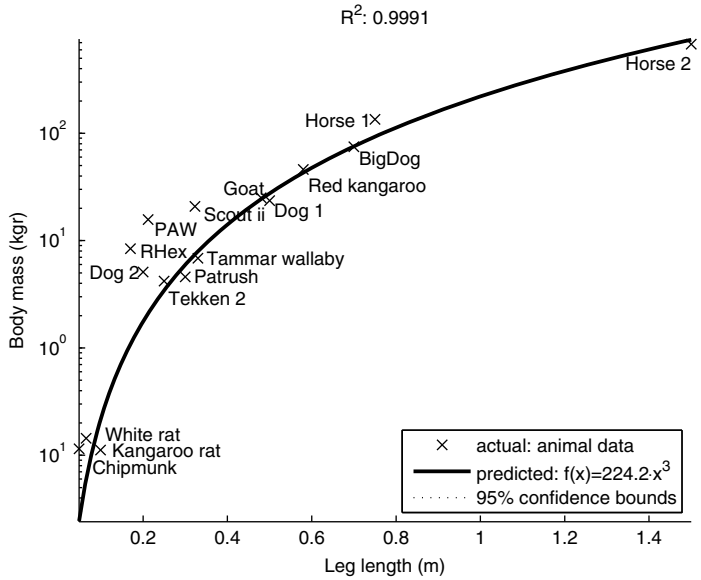

Fig. 13. Leg length vs. body mass for a series of quadruped animals.

However, the maximum permissible speed of the motor is limited by the gearbox maximum input speed and thus this implies a lower limit to length ratio. Forcing the operating speed to be less than the maximum permissible, which is scaled with motor size according to Table 3, yields the minimum length ratio $L_{\min}$ as

$$\sqrt{\frac{1}{l_o}} i_g \omega^* \leqslant \sqrt{\frac{1}{s_m}} \omega_g^* \Rightarrow L_{\min} = \left.\frac{l_o}{s_m}\right|_{\max} = \left(\frac{i_g \omega^*}{\omega_g^*}\right)^2. \tag{51}$$

Apparently, the greatest between (50) and (51) applies.

An electric motor's maximum continuous operating torque is limited by environmental factors and specifically by the amount of heat that can dissipate. Therefore, the maximum required torque should be kept below the maximum permissible motor torque (see Table 3 how it scales with motor size). This assumption leads to the maximum mass ratio $M_{\max}$ as

$$\frac{m l_o \tau^*}{i_g n_g} \leqslant m_m s_m \tau_{\max}^* \Rightarrow M_{\max} = \left.\frac{m}{m_m}\right|_{\max} = \frac{i_g n_g \tau_{\max}^*}{\tau^*} L_{\min}^{-1}. \tag{52}$$

Realistic designs require that the minimum between the values given by (48) and (52) is selected for the mass ratio. Otherwise, the overall robot mass will be either way above the target mass, even if the design is feasible, or the motor will operate overloaded.

Having calculated the length ratio L and mass ratio M from (50) or (51) and (48) or (52), respectively, the maximum payload of the robot can be evaluated. By payload we mean the sum of structural mass and the load the robot may carry. We resort to this choice so as not to assign a particular value to the structural mass and the load since different designs and materials used may lead to slightly different overall structural mass even if the shape and size of the robot is similar. The net load that the robot may carry is then the difference between the maximum payload obtained and the actual structural mass of the robot. Furthermore, one may not be interested is assigning a particular value to the carrying load, for example as in surveillance applications. To this end, the maximum payload m_p is given as the sum of structural mass m_r and the net payload the robot may carry m_l and results by subtracting the total mass of the four actuators (one at each hip), which is the sum of the motor mass m_m and gearbox mass m_g, from the target robot mass m, namely

$$m_p = m_r + m_l = m - 4(m_m + m_g). \tag{53}$$

The Curve Fitting Toolbox of MATLAB technical software package and data from a series of precision planetary gearboxes [28] are used to fit the reduction ratio to unit motor mass increase. This is illustrated in Fig. 14. Gearbox mass can be then lumped in motor mass using (54)

$$m_m + m_g = m_m \left(1 + \left(\frac{g_p}{124.6}\right)^{\frac{1}{5}}\right). \tag{54}$$

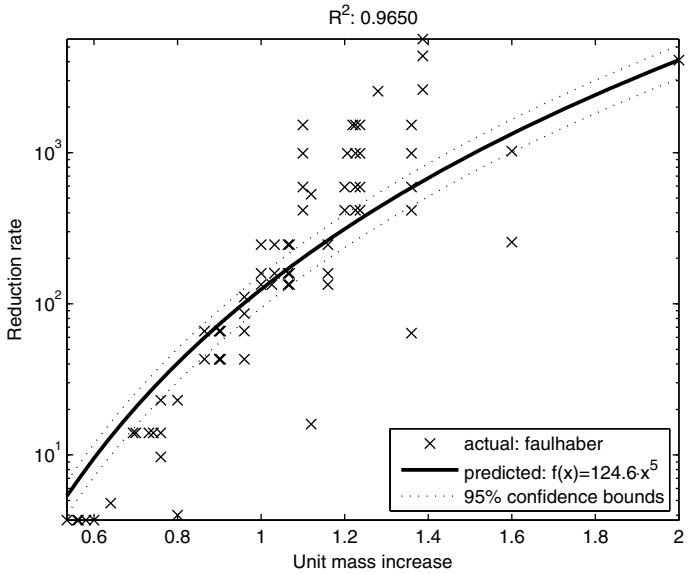

Fig. 14. Unit mass increase vs. reduction ratio for a series of commercially available precision planetary gearheads [28].

Combining (53) with (54) results to,

$$\frac{m_{\mathrm{p}}}{m_{\mathrm{m}}} = M - 4\left(1 + \left(\frac{g_{\mathrm{p}}}{124.6}\right)^{\frac{1}{5}}\right). \tag{55}$$

Eq. (55) will be used next for calculating the maximum payload over a range of actual motor and gearbox combinations.

10. Performance index and example results

Following the methodology presented in Sections 7 and 9, we seek here the optimal configuration and size for a quadruped robot with a *target mass m* of 10 kg. The motors compensate for the lost energy for the robot to execute an active gait, very close to the passive gait, which is described by (25)–(30) by exerting a constant torque, as discussed earlier. The

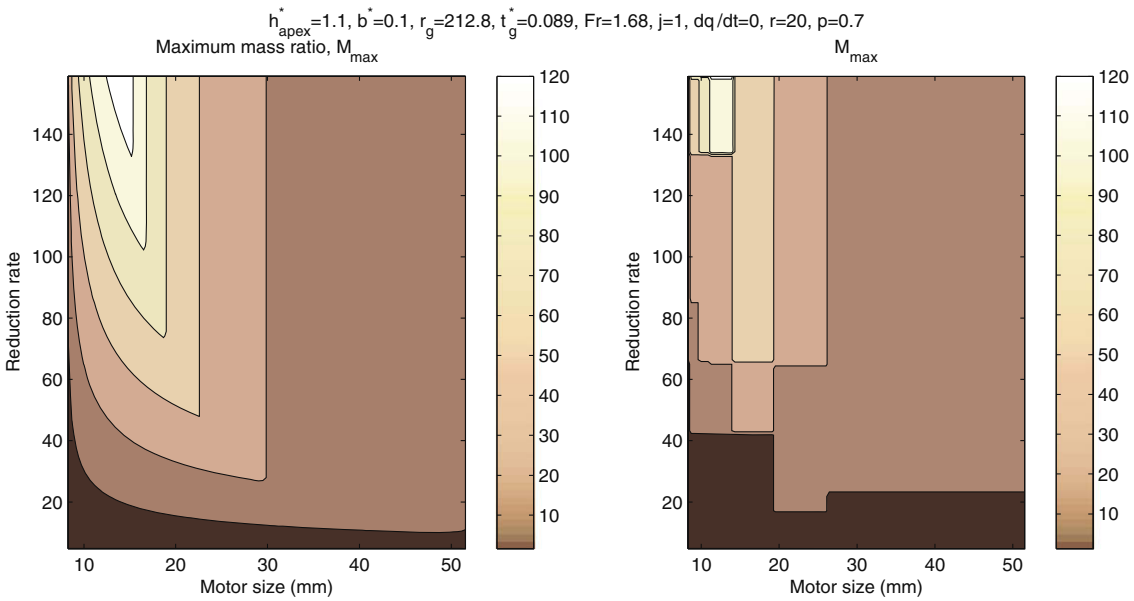

Fig. 15. Left: The maximum mass ratio for a range of motor/gearbox combinations. Right: The effect of applying actual data from a series of commercially available electric drives [28].

characteristics of the gait, i.e., apex height and pitch rate, the properties of the ground surface and the physical parameters of the system are shown in the title of each figure. Note that the dimensional form of the parameters is given. This procedure identifies the minimum size of robot actuators and connects the size of the motor drive to the size of the legged robot. In addition, the maximum permissible payload that the robot can carry for a specific overall mass is determined. To unveil of how the maximum mass ratio and the maximum permissible payload changes across a typical region of motor and gearbox physical parameters, we use (48)–(55) successively.

Specifically, by using (48) the value of the mass ratio M is calculated for a range of motor/gearbox combinations. Next, the length ratio L is calculated from (50), where motor equivalent density ρ_{m} is derived from motor data (Table 3) and robot equivalent density is estimated by Fig. 13, as discussed in Section 9. In case that this value is less than the minimum permissible length ratio $L_{\min}$, see (51), the latter is selected. In that case, the mass ratio is recalculated. The final step requires that the resulting mass ratio is checked to be less than the maximum permissible mass ratio $M_{\max}$, see (52), due to the maximum continuous operating torque of the motor. The minimum between (48) and (52) is ultimately selected.

The findings regarding the maximum mass ratio are demonstrated in Fig. 15 (left) for a range of motor/gearbox combinations, while the effect of applying actual data from a series of commercially available electric drives [28], i.e. discretization, is shown in Fig. 15 (right). Similarly, the maximum permissible payload is presented in Fig. 16 for the same range both of motor/gearbox combinations (left) and commercially available electric drives (right). Even though for the continuous data there exists a considerable number of applicable motor/gearbox combinations, in real world applications only a few combinations are practically feasible given the fact that there is not an infinite number of motor/gearbox combinations.

Although maximization of the payload is desired, we introduce a performance index that includes also the power consumption required to sustain the motion and forward speed. Power consumption is connected to energy consumption and autonomy and thus it is of great importance for legged robot applications. Forward speed is also of significant importance, since we do not want to favor slow and/or small robots. To this end, the performance index is defined as the weighted sum of relative payload, i.e., divided by the maximum permissible, and relative cost of locomotion, which was defined in (40), namely

$$\mathrm{P.I.} = w_{\mathrm{e}} \frac{\min(e^*)}{e^*} + w_{\mathrm{p}} \frac{m_{\mathrm{p}}}{\max(m_{\mathrm{p}})}. \tag{56}$$

By using (56) one can identify that combination of robot dimensionless parameters, for which the P.I. is least, and thus obtain the optimal configuration and size of the robot and the smallest actuator size that meets power requirements.

The variations on the value of a P.I., with equal weights, i.e. $w_{\mathrm{e}} = w_{\mathrm{m}} = 0.5$, over the parametric range of leg relative stiffness r and dimensionless half hip separation p, are given in Fig. 17. Leg relative stiffness and dimensionless half hip separation are chosen as the most representative is robot design since a unit dimensionless inertia is adopted inspired by [21], where a quadruped model was studied for the pronking gait in the plane. Recall that the characteristics of the gait, the properties of the ground surface and the rest robot parameters are shown in the title of Fig. 17 in their dimensionless form. It is evident from Fig. 17 that some parametric regions, marked with stars, are more desirable than others, and thus can facilitate

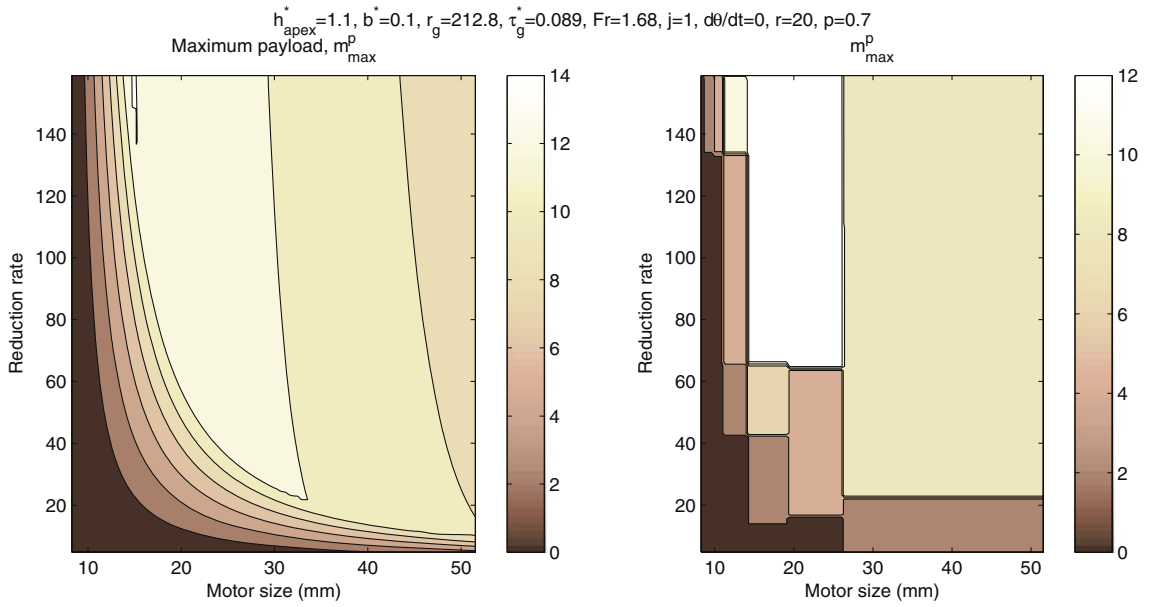

Fig. 16. Left: The permissible payload for a range of motor/gearbox combinations. Right: The effect of applying actual data from a series of commercially available electric drives [28].

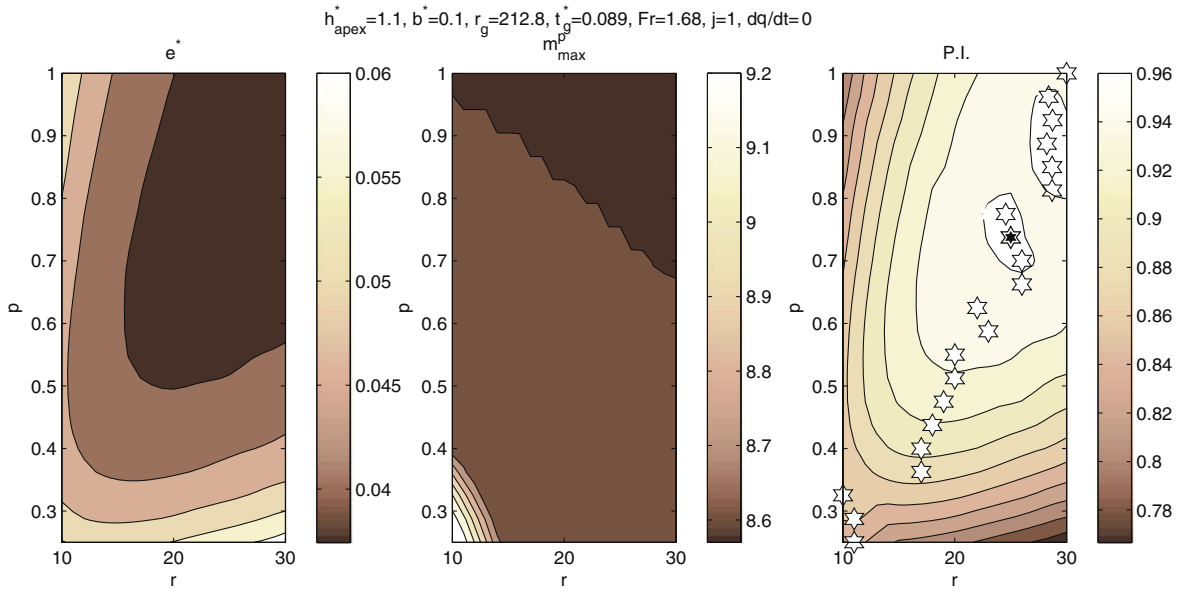

Fig. 17. Energetics, maximum payload and P.I. changes across the parametric region of the robot dimensionless parameters. Actual data from commercial drives [28] have been applied.

Table 4
Resulting robot physical parameters

Parameter	Symbol	Value	Units
Motor mass	m_m	19.00×10^{-3}	kg
Motor characteristic length	s_m	34.08	mm
Reduction rate	g_p	43.00	–
Robot mass	m	10.00	kg
Maximum payload	m_p	8.625	kg
Leg relative stiffness	r	25.00	–
Dimensionless hip separation	p	0.7431	–
Leg rest length	l_o	0.3661	m
Leg spring stiffness	k	3.349×10^3	N/m
Body length	d	540.0×10^{-3}	m
Body inertia	j	2.917	kg m^2

improved robot design. Particularly, for the selection denoted with the double star, the P.I. is maximized and thus the choice of robot parameters is optimal.

The robot physical parameters can then result by using (14)–(16) and are listed in Table 4. The resulted leg length is 366.1 mm, while body length is 540.0 mm, and compared to existing quadruped robots, it seems that the proposed configuration is rather a *tall and thin* one bringing to mind, with respect to proportions, the *Pronghorns*, the true American speedsters, which are the only animals built both for speed and endurance, while most animals are built for either speed or endurance [29]. This is a very interesting result, which suggests that the results of the analysis presented in this work can also explain some biological designs found in nature.

11. Conclusions

This work sets the basis for a systematic approach in designing quadruped robots. Dimensional analysis of a dynamically stable quadruped running in the sagittal plane with a bounding gait was employed. The findings derived from extensive simulation suggest design guidelines related to the shape of the legged robot, i.e., the optimal proportions between its physical parameters. The physical magnitude of the robot is determined through an optimization scheme using the said parametric study and commercially available motor and gearbox data. The desired performance criteria were: (a) minimization of the actuator effort to sustain a certain motion, very close to a passive one, and (b) maximization of payload capability of the robot, for a target robot overall mass. Forward speed was normalized to body length in order not to favor bigger robots. The parametric analysis presented examined the behavior of the introduced performance index over a range of non-dimensional

robot parameters, gait characteristics and practical motor/gearbox combinations. Data from experimental biology and ground surface properties were taken into consideration. The simulation results are encouraging and the proposed methodology is anticipated to assist with the design of new quadruped robots, as well as the modification of existing ones.

Acknowledgement

Support by public (European Social Fund 80% and General Secretariat for Research and Technology 20%) and private funds (Zenon SA), within measure 8.3 of Op. Pr. Comp., 3rd CSP-PENED 2003, is acknowledged.

References

[1] M.H. Raibert, Legged Robots that Balance, MIT Press, Cambridge, MA, 1986.
[2] J.G. Nichol, S.P.N. Singh, K.J. Waldron, L.R. Palmer III, D.E. Orin, System design of a quadrupedal galloping machine, Int. J. Robot. Res. 23 (10–11) (2004) 1013–1027.
[3] I. Poulakakis, E. Papadopoulos, M. Buehler, On the stability of the passive dynamics of quadrupedal running with a bounding gait, Int. J. Robot. Res. 25 (7) (2006) 669–687.
[4] R. Playter, M. Buehler, M. Raibert, BigDog, in: G.R. Gerhart, C.M. Shoemaker, D.W. Gage (Eds.), Proc. of SPIE Defense & Security Symposium, vol. 6230, Unmanned Systems Technology VIII, 2006.
[5] J.A. Smith, I. Sharf, M. Trentini, Bounding gait in a hybrid wheeled-leg robot, in: IEEE/RSJ Int. Conf. on Intelligent Robots and Systems (IROS), Beijing, China, October 2006.
[6] Zu Guang Zhang, Hiroshi Kimura, Yasuhiro Fukukoka, Self-stabilizing dynamics for a quadruped robot and extension towards running on rough terrain, J. Robot. Mechatron. 19 (1) (2007) 3–12.
[7] H. Kimura, Y. Fukuoka, A.H. Cohen, Adaptive dynamic walking of a quadruped robot on natural ground based on biological concepts, Int. J. Robot. Res. 26 (5) (2007) 475–490.
[8] P. Chatzakos, E.G. Papadopoulos, Parametric analysis and design guidelines for a quadruped bounding robot, in: Proc. of the 15th Mediterranean Conf. on Control and Automation, Greece, 2007.
[9] W.J. Duncan, Physical Similarity and Dimensional Analysis, Edward Arnold, London, 1953.
[10] O. Reynolds, An experimental investigation of the circumstances which determine whether the motion of water shall be direct or sinuous, and of the law of resistance in parallel channels, Philos. Trans. Roy. Soc. 17 (1883) 935–982.
[11] Froude number, in Encyclopaedia Britannica. From Encyclopaedia Britannica Online: <http://www.britannica.com/eb/article-9035514>.
[12] R.McN. Alexander, Terrestrial locomotion, in: R.McN. Alexander, G. Goldspink (Eds.), Mechanics and Energetics of Animal locomotion, Chapman and Hall, London, 1977.
[13] R.J. Full, D. Koditschek, Templates and anchors: Neurome–chanical hypotheses of legged locomotion in land, J. Experiment. Biol. 202 (1999) 3325–3332.
[14] M. Ahmadi, M. Buehler, Stable control of a simulated one-legged running robot with hip and leg compliance, IEEE Trans. Robot. Automat. 13 (1) (1997) 96–104.
[15] E. Papadopoulos, N. Cherouvim, On increasing energy autonomy for a one-legged hopping robot, in: Proc. of the IEEE Conf. on Robotics and Automation, 2004, pp. 4645–4650.
[16] N.C. Heglund, C.R. Taylor, Speed, stride frequency and energy cost per stride: How do they change with body size and gait?, J Experiment. Biol. 138 (1988) 301–318.
[17] U. Saranli, M. Buehler, D.E. Koditschek, RHex: a simple and highly mobile hexapod robot, Int. J. Robot. Res. 20 (7) (2001) 616–631.
[18] P.P. Gambaryan, How Mammals Run: Anatomical Adaptations, Wiley, New York, 1974.
[19] K.H. Low, Bai Shaoping, Terrain-evaluation-based motion planning for legged locomotion on irregular terrain, Adv. Robot., Japan 17 (8) (2003) 761–778.
[20] S. Barry, Scaling laws for mesoscale and microscale systems, IEEE Trans. CPMT – Adv. Packag., 1999.
[21] M.D. Berkemeier, Modeling the dynamics of quadrupedal running, Int. J. Robot. Res. 17 (9) (1998) 971–985.
[22] R. Blickhan, The spring-mass model for running and hopping, J. Biomech. 22 (1989) 1217–1227.
[23] C.T. Farley, J. Glasheen, T.A. McMahon, Running springs: speed and animal size, J. Experiment. Biol. 185 (1993) 71–86.
[24] H.M. Herr, G.T. Huang, T.A. McMahon, A model of scale effects in mammalian quadrupedal running, J. Experiment. Biol. 205 (2002) 959–967.
[25] G. Gabrielli, T. von Karman, What price speed? Specific power required for propulsion of vehicles, Mech. Eng., ASME 72 (10) (1950).
[26] R.M. Alexander, Principles of Animal Locomotion, Princeton University Press, 2003.
[27] N. Cherouvim, E. Papadopoulos, Energy saving passive-dynamic gait for a one-legged hopping robot, Robotica 24 (4) (2006) 491–498.
[28] www.faulhaber-group.com, Brushless DC Servomotors.
[29] J.A. Byers, Built for Speed, A Year in the Life of Pronghorn, Harvard University Press, 2003.